Ultrafast Science
A SCIENCE PARTNER JOURNAL

REVIEW ARTICLE

Ultrafast Laser Filamentation in Transparent Solids

Tianyang Yan[1] and Lingfei Ji[2,3]*

[1]Pen-Tung Sah Institute of Micro-Nano Science and Technology, Xiamen University, Xiamen 361005, China. [2]Institute of Laser Engineering, Faculty of Materials and Manufacturing, Beijing University of Technology, Beijing 100124, China. [3]Key Laboratory of Trans-scale Laser Manufacturing Technology, Ministry of Education, Beijing 100124, China.

*Address correspondence to: ncltji@bjut.edu.cn

Citation: Yan T, Ji L. Ultrafast Laser Filamentation in Transparent Solids. *Ultrafast Sci.* 2023;3:Article 0023. https://doi.org/10.34133/ultrafastscience.0023

Submitted 2 March 2023
Accepted 6 July 2023
Published 1 August 2023

Ultrafast laser filamentation results from the interaction of ultrafast laser with Kerr media. During filamentary propagation, the transparent medium is altered by numerous linear and nonlinear effects of ultrashort laser pulses. Filamentation can cause material modification in solids through laser energy deposition and ionization processes, which creates a new opportunity for ultrafast laser processing of materials when combined with filamentary propagation characteristics, such as intensity champing and long propagation distance. This paper reviews the research on ultrafast laser filamentation in solids for micro- and nano-processing, including the fundamental physics, filamentation characteristics, and applications in solids for ultrafast laser filamentation-induced processing. Additionally highlighted are the difficulties and potential applications for solid-based filamentation-induced processing.

Introduction

The laser beam can overcome the diffraction effect when the peak power of the ultrafast laser is larger than the self-focusing threshold, and self-guided propagation [1] occurs. As illustrated in Fig. 1A, in the self-guided way, the ultrafast laser excites ionization after self-focusing, resulting in the plasma with a certain transverse density gradient. When the plasma-defocusing and self-focusing effects balance dynamically, a plasma channel called filamentation [2,3] is produced. The initial discovery of filamentation occurred in the 1960s [4], and Q-modulated laser pulses produced a string of damages with a diameter of several micrometers in the glass. Benefited from the advancement of laser-chirped pulse amplification technology [5], Braun et al. [1] freely incident the femtosecond (fs) laser pulses into the air, producing filamentation with a length of more than 20 m in 1995. Since then, ultrafast laser filamentation has emerged as a well-liked subject of research in applied physics [6–9].

While the fundamental principles of ultrafast laser filamentation have been well studied in gases and liquids, the physical properties of solid media, such as low spatial freedom and low electrical conductivity, have made investigating the evolutionary laws and intrinsic mechanisms of filamentation in solids difficult. As shown in Fig. 1B, the dynamic balance between self-focusing and plasma defocusing effects in solids makes the spatial distribution of the filamentary plasma inhomogeneous. Moreover, the nonuniform refractive index perturbations [10] and complicated intensity-clamping effect [11] in solids make modulating filamentation difficult. Nevertheless, the plasma density generated by ultrafast laser filamentation in solids is typically higher than in gases and liquids. Higher plasma density causes greater pulse energy absorption, which can cause permanent changes or structural damage to the material, as shown in Fig. 1C, offering an opportunity for high-precision processing by ultrafast laser filamentation. Ultrafast laser filamentation in solids has been employed effectively to fabricate waveguide devices and grating constructions, precision cutting, drilling, and other applications [12].

The primary scope of this paper is to introduce the advancement in ultrafast laser filamentation-induced micro/nano-processing in solids, ranging from filamentation characteristics and propagation mechanisms in solids to the filamentation processing strategy and applications, as well as outline the difficulties and opportunities toward the filamentation-induced micro/nano-processing in solids. The "Characteristics and modulations of filamentation in solids" section begins by discussing the filamentation characteristics and modulation strategies. The "Propagation model of filamentation in solids" section covers the nonlinear propagation models and balance mechanism of the filamentation in solids. An overview of the ultrafast laser filamentation-induced processing technology and applications in solids is given in the "Applications of filamentation in transparent solids for micro/nano-processing" section. Finally, the difficulties and prospects of filamentation-induced processing are discussed.

Characteristics and modulations of filamentation in solids

In all transparent media, an extraordinary nonlinear optical phenomenon called filamentation emerges during ultrafast

laser with a high peak power propagation. Because of different free electron generation processes, laser parameters, and unique physical and optical properties of solids, there is a noticeable variance in filamentation characteristics. The main dynamic balancing factors and the nonlinear propagation model also differ marked. Understanding filamentation characteristics facilitate modulating filamentation and the development of filamentation applications in solids.

Intensity clamping

The positive refractive index change ($\Delta n = n_2 I(r,t)$) is generated by the self-focusing effect, and the negative refractive index change ($\Delta n = -\rho(r,t)./.2\rho_c$) is caused by the plasma defocusing effect. The self-focusing effect impacts the plasma density. In turn, the plasma defocusing phenomenon restricts the self-focusing effect. When the self-focusing and plasma defocusing effects establish a dynamic balance, filamentation is limited in optical intensity and diameter. This phenomenon is called intensity clamping [13,14]. Supercontinuum spectroscopy and the morphology of the modified material can demonstrate the intensity clamping effect in solids. Liu et al. [11] produced supercontinuum spectra in soda lime glass using fs laser filamentation with a pulse duration of 170 fs and a wavelength of 800 nm. As demonstrated in Fig. 2A, the minimum wavelength (blue dot line, ~400 nm) remains almost constant over this range of input laser energies, and the central wavelength (red dot line, ~800 nm) is found to remain constant. The maximum blue shift caused by self-phase modulation is not dependent on the pulse energy (20 μJ). This implies that the filamentation intensity is limited to a specific range. In Fig. 2B, Amina et al. [15] induced a filamentation-modified trace with a total length of about 1,028 μm in sapphire using a picosecond (ps) laser pulse with a pulse duration of 10 ps and a wavelength of 355 nm. Despite the obvious crack damage at the initiation position of the filamentary trace (near the geometric focusing position) and isolated modified dots at the tail position of the filamentary trace due to gradual energy loss, the appearance of relatively long (~880 μm) modified traces of uniform diameter and relatively uniform modification type at the intermediate position indicates that the filamentation not only maintains the energy density over a certain propagation distance but also limits the laser beam diameter expansion.

Long propagation distance

Ultrafast laser is more accessible to induce the self-focusing effect (the critical threshold $P_{cr} = 3.77\lambda_0^2 / 8\pi n_0 n_2$, where λ_0 denotes the wavelength and n_0 and n_2 are the refraction index and nonlinear refractive index coefficient, respectively [16]) in solids than in the air because solids have higher linear and nonlinear refractive indices than air. However, solids have a high atomic density, and the plasma density in the filamentation usually reaches 10^{18} to 10^{21} cm^{-3} [17–19], which is much higher than the plasma density in the air (~10^{16} cm^{-3}) [20,21]. Compared to air, the solid has a higher group velocity dispersion (GVD) coefficient. The peak power of the ultrafast laser rapidly drops below P_{cr} in solids due to energy loss induced by larger plasma density and an increase in pulse duration produced by a larger GVD coefficient, thereby early terminating the filamentary propagation.

Extending filamentary propagation in solids is commonly accomplished by changing laser parameters like pulse energy, wavelength, repetition rate, pulse number, and pulse duration. In fused silica [22] and polymethyl methacrylate (PMMA) [23], increasing the pulse energy of the fs laser or the irradiation pulse number can expand the filamentary propagation distance. Nevertheless, it is followed by an uneven modification and discontinuous diameter of the filamentary traces induced by the unstable energy absorption of the modified material. When the peak power exceeds P_{cr} by a significant amount, modulation instability can lead to unstable multiple filamentations [24,25] and optical breakdown [26]. At a given peak intensity, the filamentation length increases with pulse duration [27]. For few-ps duration pulses, the filamentation decays rapidly at the surface. In contrast, a new filamentation occurs after a long propagation of the filamentation with a longer pulse duration. This is because longer pulse duration pulses can be self-focused over a longer period, causing the energy to converge again. The effect of laser wavelength on filamentary propagation distance is primarily due to the slowing of the pulse duration broadening by abnormal GVD and the appearance of the refocusing phenomenon, which causes the propagation distance to increase with wavelength [28,29]. With the repetition rate (about kilohertz level) decreasing, the filamentary propagation distance expands [30]. The smaller pulse time interval leads to a more pronounced pulse accumulation effect, resulting in the imprecise modified regions along the filamentary propagation axis,

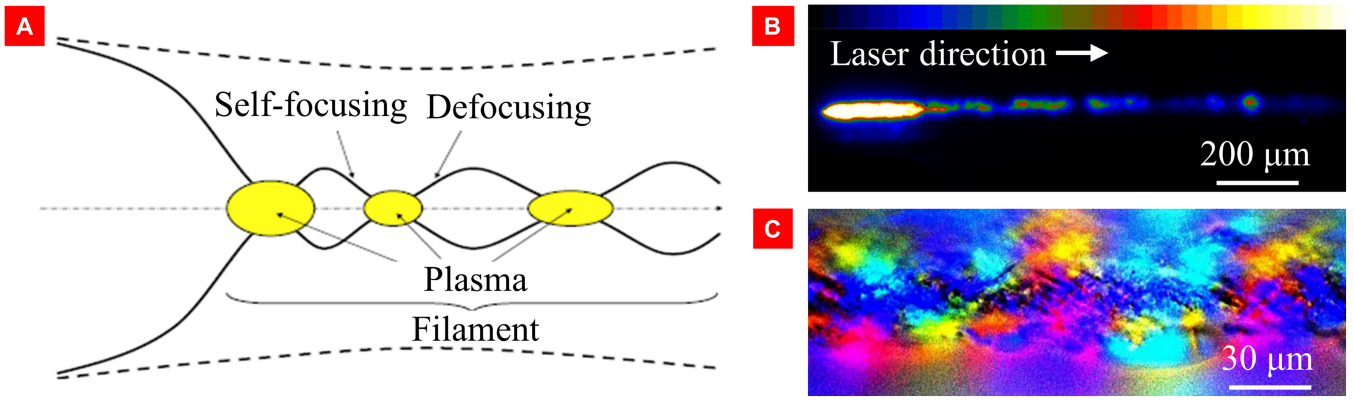

Fig. 1. (A) Schematic diagram of self-guide mode [3]. (B) ICCD micrograph of filamentary plasma induced by wavelength 355 nm ps laser in sapphire. (C) Magnified cross-polarized microscopy images of the filamentation-induced modified region.

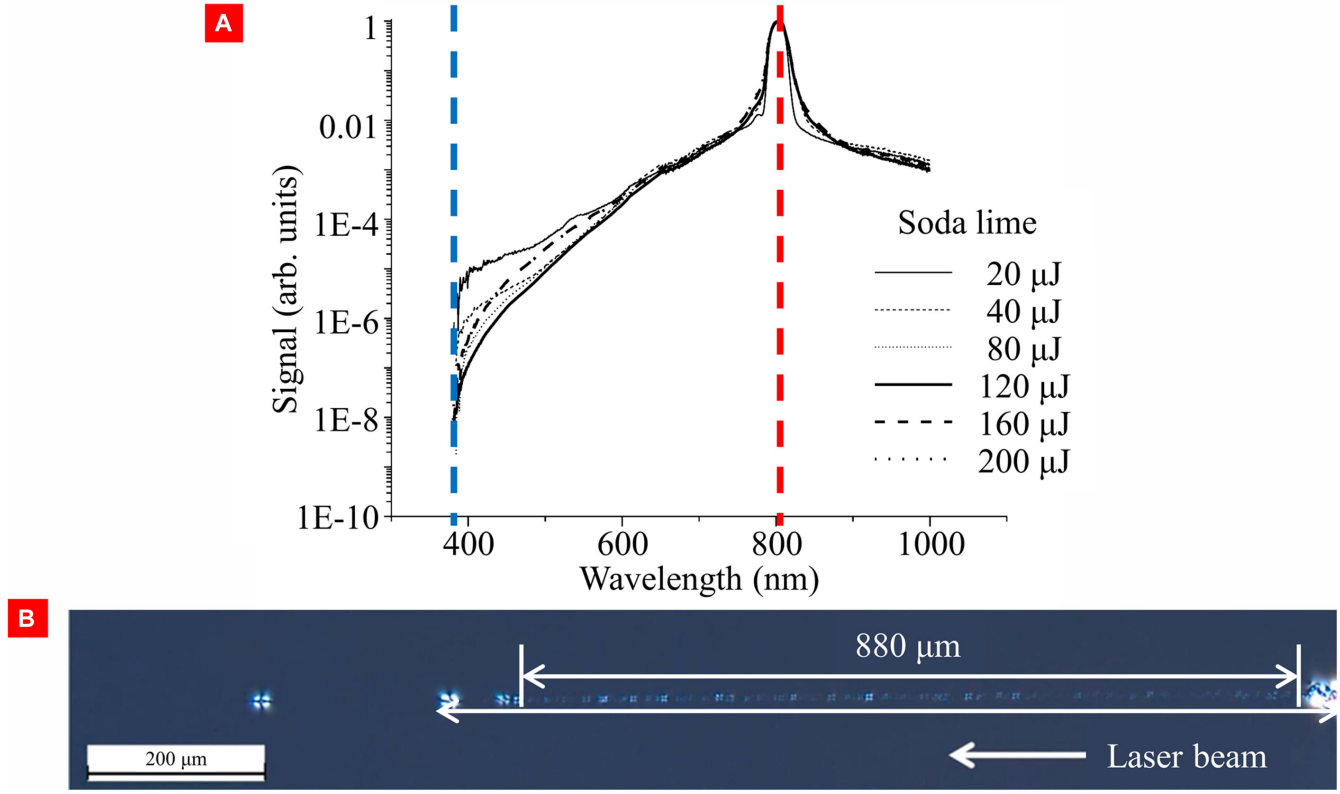

Fig. 2. (A) Spectra obtained fs laser filamentation in glass at various pulse energies [11]. (B) Microscopic image of the filamentary trace with a length of 1180 μm induced by ps laser pulses in sapphire [15].

which prevents the energy supplement by the background energy reservoir.

Maintaining the plasma life is one method for extending filamentary propagation because filamentation is a plasma channel [31,32]. In Fig. 3A, Ji and colleagues [33] induced filamentary modified traces with a maximum length of 833.3 μm in sapphire by the ps laser burst (sub-pulse time interval, ~50 ns) containing the various sub-pulse number and energies. The

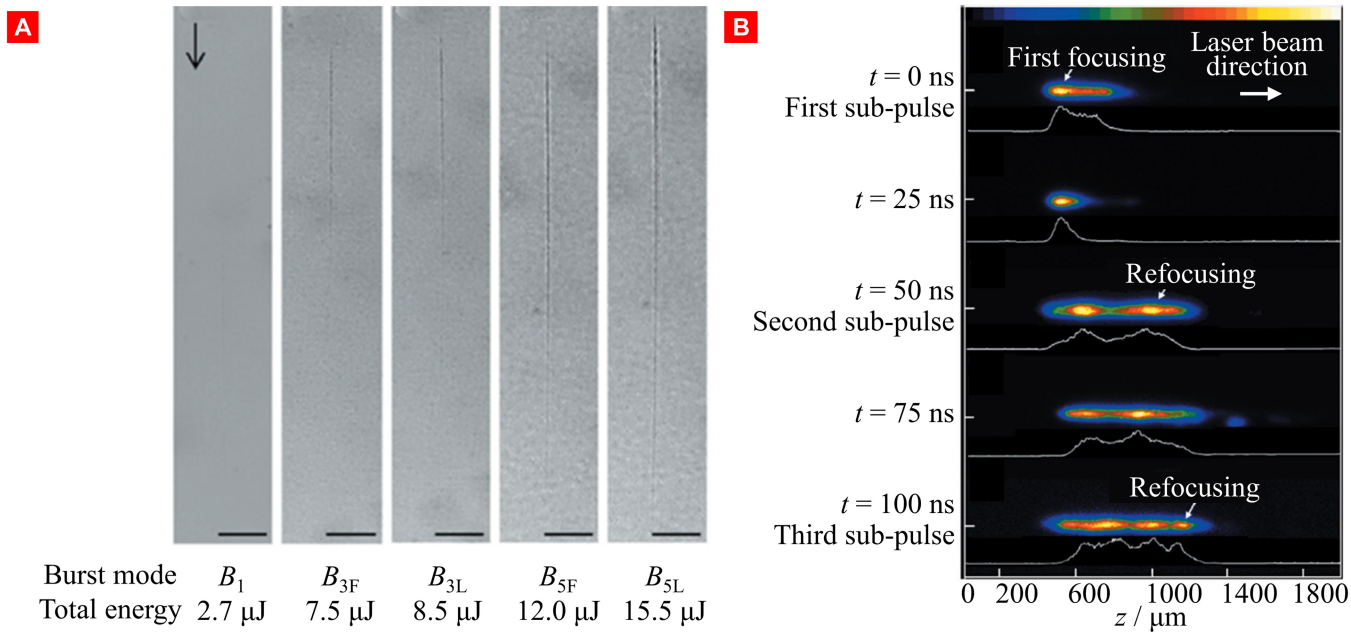

Fig. 3. (A) Influence of different burst modes on the morphology of the filamentary trace. Scale bars, 100 μm. (B) Instantaneous morphology of filamentary plasma caused by ps laser burst at various times [33].

instantaneous images of the filamentary plasma demonstrate that the plasma peak created by the succeeding sub-pulse follows the previous plasma peak and appears at the lower plasma density zone in the filamentary plasma string, as shown in Fig. 3B. The uniformity and distance of the plasma channel are essentially improved by subsequent sub-pulses, which produce plasma peaks with more spatial overlap. Moreover, Ji and colleagues [34] investigated the atmospheric influence on ps laser filamentary propagation. The primary factor affecting the sapphire surface plasma is the thermal conductivity of the gas. The expansion volume of the surface plasma can be actually decreased by higher thermal conductivity gases, enabling more pulse energy to support filamentary propagation. Compared with Ar and N_2, O_2 has the highest thermal conductivity, with the most extended filamentary trace in sapphire.

Background energy reservoir

Through filamentation blocking experiments by various diameter pinholes, Liu et al. [35] intuitively highlighted the important significance of background energy reserve in the whole filamentary propagation process. The filamentary propagation distance is extended when the filamentation passes through the pinholes with larger diameters. This indicates that the primary energy to maintain the nonlinear propagation comes from the background region of filamentation, which serves as a reservoir of the energy [36]. Once the peak power in the background energy reservoir exceeds P_{cr}, a single filamentation can split into multiple filamentations due to modulation instability [37,38].

The discovery of the background energy reservoir provides a theoretical foundation for regulating the filamentary propagation distance and managing multiple filamentations. By customizing the annular beam profiles, Wang et al. [39] achieved control of the initial and ending positions of fs laser filamentation in the glass. The energy distribution of the laser beam was shaped by the iris diaphragm ring and amplitude mask. The initial position of the filamentation was controlled by the inner diameter of the ring laser beam, as shown in Fig. 4, and the ending position was defined by the outer diameter of the ring laser beam. Wang and colleagues [40] proposed using phase-nested beams to significantly extend (~7.6 times) filamentary propagation distance in BK7 glass. A single phase-nested beam was assembled by filamentation and subsequent energy replenishment. The central part of the laser beam is focused to produce a shorter filamentation. The energy required for the extension into filamentary propagation is supplemented by the energy of the rest of the annular part. Hou and colleagues [41] built a feedback-based wavefront shaping system with an annular phase mask to tune the initial and ending position of fs laser filamentation. The different energy ratios of the annular region can adjust the length and spatial position of filamentation in K9 glass.

To avoid the generation of unstable multiple filamentations in solids, researchers have proposed a series of methods to produce a stable background energy reservoir. Based on the amplitude modification of different wavefronts, such as microlens array [42], the highly elliptical beam [43], 2 or 3 beams interfere [44], and wedge plate [45] are adopted. Li et al. [46] used the fs vortex laser beams with collinear interfere to obtain controllable annular multiple filamentations. The pattern and rotation of the filamentations were well controlled with the topological charges and delay time of 2 laser beams, as shown in Fig. 5A and B. Further research shows that the multiple filamentation

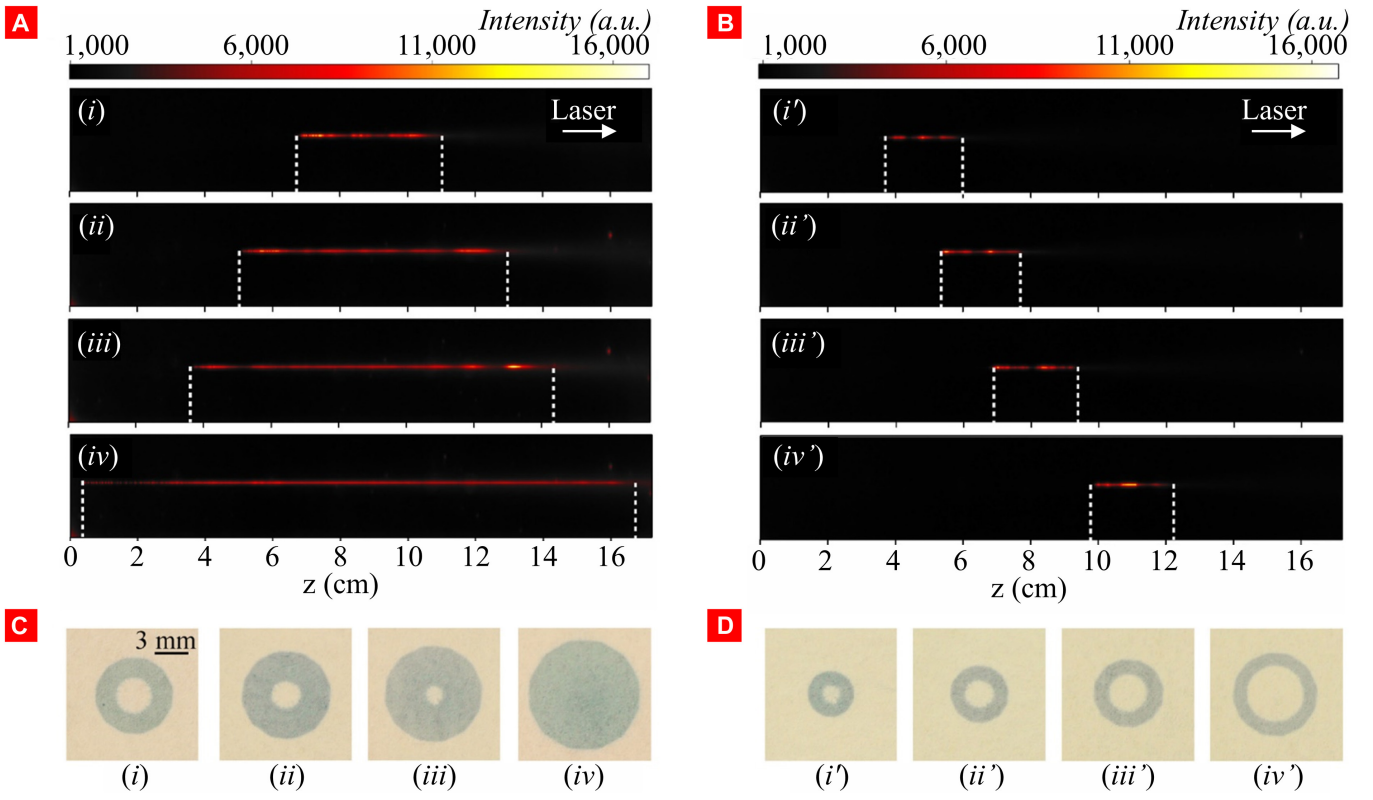

Fig. 4. (A and B) Influence of the outer and inner diameter on the initial and ending position of filamentation. (C and D) Laser beam profiles [39].

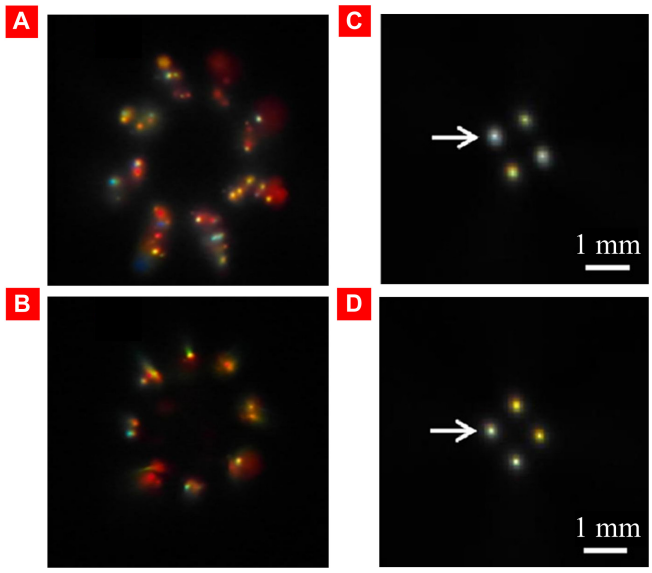

Fig. 5. (A and B) Various distributed multiple filamentations generated by different delay times in fused silica [46]. (C and D) Multiple filamentations with different rotation angles in the fused silica [50].

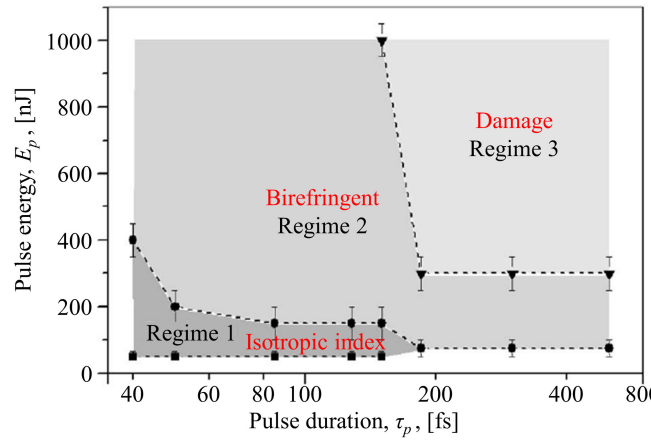

Fig. 6. Energy thresholds of different modification types under various pulse energies and pulse durations [53].

array generated by ultrafast laser with phase modulation, including the spatiotemporal delay phase [47], the binary phase mask [48], and the phase grating [49], is more stable than filamentation arrays with the amplitude modification. In Fig. 5C and D, Hao and colleagues [50] presented a method that generates regular multiple filamentations using fs vector laser beams. The topological charges of the laser beams determine the filamentation number. The necklace-like multiple filamentations in glass can be constantly rotated by changing the polarizer.

Energy transfer and modification

Pulse energy from the laser radiation field is transferred to the free electrons of the dielectric during filamentary propagation. The electrons achieve quasi-thermal equilibrium in 10^{-13} s due to electron–electron scattering. The electron energy follows the Fermi–Dirac distribution law and has a higher electron temperature than the lattice temperature. Through the outward radiation of longitudinal optical phonons, electron energy in the quasi-thermal equilibrium state is finally transferred to the lattice. Although the phonon radiation time is only 200 fs, a significant amount of phonon radiation is required to reduce energy. As a result, the electron temperature takes longer to cool, and the electron–phonon coupling relaxation time is within 10^{-13} to 10^{-12} s. The energy distribution of the phonon relaxation process then approaches the thermal equilibrium state (10^{-12} s). The energy absorption and lattice heating processes can be separated because of the shorter pulse duration of the fs laser [51]. Many hot electrons are in the cold lattice after an fs laser pulse radiation. The energy relaxation process and material structural changes are determined by the system response to the strong nonequilibrium conditions [52]. Because the time of the phonon relaxation is close to the ps laser pulse duration (~10^{-12}s), the ps laser filamentation is accompanied by a specific thermal effect [53]. When the peak power and laser wavelength are constant, the energy loss in fs laser filamentary propagation is dominated by multiphoton ionization. In contrast, ps laser filamentary propagation is dominated by avalanche absorption. Numerical calculations by Houard et al. [54] show that the pulse duration does not significantly affect the filamentation length and plasma density, but rather the hydrodynamics of filamentary propagation; specifically, the difference in the primary ionization mechanism causes the difference in the self-focusing and defocusing processes during filamentary propagation (plasma peaks appear at different locations). The fs laser filamentary propagation in transparent solids induces a refractive index change dominated by residual stresses and nano-defects, mainly by applying the refractive index change. For ps laser, filamentary propagation is accompanied by certain thermal effects, so the main focus is on the application of microcrack and melting.

As shown in Fig. 6, with increasing pulse energy and pulse duration, fs laser filamentation induced permanent isotropic refractive index change (type I), birefringence change (type II), and damage (type III) in fused silica [53,55–57]. The damage type and morphology of the filamentary trace are well-fitted by simulations of plasma density and profile. The plasma density thresholds of different modification types were determined [57]. The causes of type I modification include the thermal gradient of material [58], densification, and strain stress in glass [59]. Type II modification is related to the polarization change caused by the self-ordered nanostructures [60]. High-pressure shock waves induced by high-density plasma charge separation cause microcrack damage [61,62]. The same type of modifications was observed in filamentary traces induced by sub-ps laser pulses [22].

In crystalline materials, such as sapphire [63], $LiNbO_3$ [64], and Nd: YAG [65], there are 3 types of modified traces of fs laser filamentation. It is important to note that the partial refractive index change can be alleviated or even eliminated by annealing [63,66,67], indicating that strain stress [68] based on the enhancement of the electronic polarization index under the short-time action (~150 fs) of fs laser is one of the causes of refractive index change [69,70]. Ji and colleagues [71] investigated the modification type of sapphire induced by the ps laser filamentation. Because the relatively long pulse duration and avalanche ionization dominate the nonlinear ionization, the thermal effect in the filamentation cannot be ignored. With increasing pulse energy, 2 different modifications were found in the filamentary traces: birefringence changes and structural damages. All filamentary traces induced by the ps laser occurred

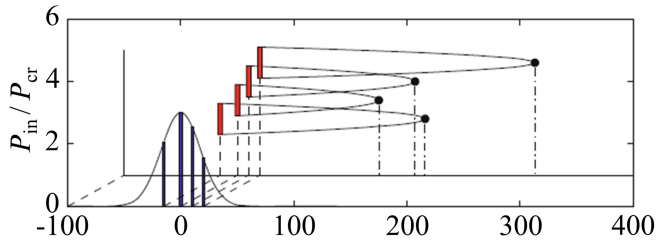

Fig. 7. Schematic diagram of moving focus mode [5].

the phase change from $\alpha - Al_2O_3$ to $\gamma - Al_2O_3$, forming irreversible ceramic-like polycrystalline microstructures with grains and pores.

Propagation model of filamentation in solids

Due to the limited plasma life, self-compression phenomenon, and spatial freedom of solids, directly measuring the temporal variation of ultrafast laser pulses in solids is a challenge. Numerical simulation is one of the powerful tools for assisting the analysis of ultrafast laser filamentary propagation in solids. Several groups have developed numerical simulations to reveal the influence of the ultrashort laser pulse on filamentation characteristics [7,72,73]. On this basis, the researchers add source terms to the model according to the experimental conditions and perform theoretical studies on the influences of various physical effects. In many papers about ultrafast laser filamentation, the nonlinear Schrödinger equation (NLSE) is solved numerically using slow amplitude approximation and paraxial approximation to solve Maxwell's equation. The specific equation of NLSE can be expressed as follows [54,74,75],

$$\frac{\partial \varepsilon}{\partial z} = \frac{t}{2k_0}\nabla_{\perp}^2\varepsilon - \frac{\alpha}{2}\varepsilon - \frac{ik''}{2}\frac{\partial^2\varepsilon}{\partial t^2} + i\frac{\omega_0}{c}n_2|\varepsilon|^2\varepsilon - \frac{\beta^{(K)}}{2}|\varepsilon|^{2K-2}\varepsilon - \frac{\sigma}{2}\left(1+i\omega\tau_c\right)\rho\varepsilon \quad (1)$$

where ε denotes the electric field envelope. t changes to $t - (z/v_g)$ in the coordinate system, in which the pulses move together with group velocity v_g. The diffraction of the laser, linear absorption of the solid, GVD, optical Kerr effect, multiphoton absorption (MPA), and plasma effects (absorption and defocusing) are described on the right-hand side of Eq. 1. ω_0 is the center angular frequency, and the center wave number k_0 is expressed as $k_0 = n_0\omega_0/c$. Laplacian operator represents the radial diffraction of the laser beam, α is the absorption coefficient of the solid, and k'' is the coefficient of GVD. ρ is the plasma density produced by multiphoton ionization (MPI) and avalanche ionization [76]. The cross-section of MPA $\beta^{(K)} = K\hbar\omega_0\sigma^{(K)}\rho_{nt}$ [73], where ρ_{nt} is the density of the neutral atom, K is the minimum number of MPA, and τ_c is the kinetic momentum transfer time.

Self-guide mode

According to the self-guiding model [1], the laser intensity increases due to the Kerr self-focusing phenomenon. When the ionization threshold of the medium is reached, the laser generates plasma through nonlinear ionization. The plasma produces the defocusing effect on the laser. When natural diffraction, plasma defocusing effect, and self-focusing effect of ultrafast laser reach dynamic balance, the ultrafast laser stimulates the filamentation. It maintains a specific beam diameter to propagate forward for a considerable distance [77]. The filamentation is described as a spatial soliton in the self-guided model. However, it does not consider that pulse and plasma density varies with temporal modulation. As a result, the self-guided model is an incomplete physical model, but it can reveal the refocusing cycle phenomenon in filamentation [78,79].

Moving focus mode

In Fig. 7, the laser pulse is split into several independent time slices, and each slice has a corresponding peak power in the moving focus mode [80]. Every time slice whose peak power exceeds P_{cr} focuses at a specific propagation distance.

The Marburger formula [16] can be used to describe the relationship between the self-focusing position and its peak power:

$$Z_f(P) = \frac{0.367kw_0^2}{\left[\left(\sqrt{P_{peak}/P_{cr}} - 0.852\right)^2 - 0.0219\right]^{1/2}} \quad (2)$$

where $k = 2\pi/\lambda_0$ denotes the wave number and w_0 is the beam waist. It is evident that the slice with the greater peak power can be focused faster. However, the filamentary propagation following the geometric focus is not explained by the moving focus model. This is because the moving focus model ignores the energy coupling of different time slices under the plasma effect. Nonetheless, the moving focus model can predict the initial position of the filamentation. When a focal length f lens focuses the ultrafast laser, the collapsed position $L_{c,f}$ of the convergent beam shifts to [36]:

$$Z_{c,f} = \frac{1}{Z_f(P)} + \frac{1}{f} \quad (3)$$

It should be noted, in particular, that when calculating the initial position of filamentation in solids, the influence of the spherical aberration of the laser from the air to the solid interface should also be considered [81]. Gong and colleagues [82–84] qualitatively explained the refocusing behavior in filamentary propagation as a function of external focusing conditions and pulse energy. The profiles of the potential wells with different focal lengths and input energies were numerically calculated. The focusing phenomenon is described by particle oscillation, and the profiles of potential wells with different time slices explain the multiple refocusing processes.

Dynamic spatial replenishment model

Mlejnek et al. [85] proposed a dynamic spatial replenishment model in 1998 that effectively combines the moving focus and self-guided models. Figure 8A shows the maximum of the on-axis intensity over time as a function of propagation distance z with different peak input powers. The model considers that self-focusing first increases the intensity of the leading part of the pulse. Ionization then generates plasma, which causes the defocusing effect on the trailing part of the pulse. Because of the plasma defocusing and MPA, the pulse energy of the leading part decreases until the solid cannot be ionized, as shown at z = 55 cm in Fig. 8B. Figure 8C shows the transformed normalized electric field sample profiles. At z = 55 cm, the beam power is shifted into a spatial ring due to defocusing effect. Due to the still active self-focusing effect, the trailing

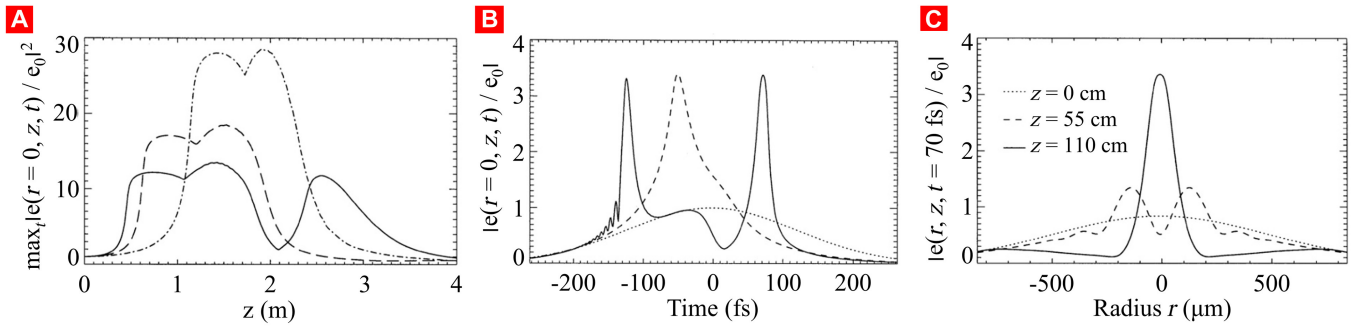

Fig. 8. (A) Global maximum over time of the on-axis intensity as a function of propagation distance z for peak input powers of $5.5P_{cr}$ (dashed-dotted curve), $6.0P_{cr}$ (dashed curve), and $6.5P_{cr}$ (solid curve). (B and C) On-axis normalized field amplitude as a function of time and transverse normalized electric field amplitude profiles, at which the trailing pulse forms for $z = 0$ (dotted curve), 55 (dashed curve), and 110 cm (solid curve), for peak input power $6.5P_{cr}$ [85].

part of the pulse gathers energy to the center at $z = 110$ cm. This results in a cycle of focusing and defocusing.

Until now, no model has been able to encompass all the physical connotations of filamentation. The initial laser conditions and the medium properties influence filamentary propagation, and a specific propagation model is usually dominant. The formation of fluorescent tracks of filamentation in single fs laser pulses in LiF crystal, for example, is adequately described by the classical moving focus model. The contribution of plasma defocusing terms is relatively small [86]. The experimental results of filamentary propagation by infrared (wavelength of 1,550 nm) fs laser pulses in silica induced show that anomalous GVD favors a longer self-guiding [29]. The main factors that balance the self-focusing effect also change. The long-distance filamentary propagation mechanism of an 800 nm infrared fs pulse in fused silica was studied by Tzortzakis and colleagues [77]. They emphasized that the self-guided mode is a dynamic balance of MPI and self-focusing. Bergé and colleagues [87] clarified the roles of GVD, MPA, and plasma defocusing of fs laser filamentation in fused silica. If the normalized GVD length is smaller than the power ratio (input peak power/self-focusing threshold), the dispersion arrests the collapse of the pulse. MPA saturates the Kerr effect at low wavelengths and stabilizes the laser beam to propagate long distances without the plasma defocusing effect. In high-numerical aperture (NA) conditions, Richardson and colleagues [88] proposed that geometrical focusing and plasma effects are the main factors that govern filamentation. Kerr self-focusing effect plays an important role as NA decreases. Dubietis and colleagues [17] presented that the space–time conversion of the ps pulse is dominated by plasma, whereas fs laser filamentation is driven by MPA. The density of filamentary plasma stimulated by the 1,064 nm ps laser in sapphire was studied by Ji and colleagues [89]. The avalanche ionization rate increases faster than the photoionization rate with the ps pulse energy. The essential role of avalanche ionization in the ps laser filamentation was revealed. Nagar et al. [90] reported an anomalous regime caused by wavelength (1.2 to 2.3 μm) dependence of the electron collision time for laser filamentation in fused silica. The electron collision times decrease (<1 fs) with the wavelength increase because of the generation of hotter electrons via ponderomotive heating at longer wavelength filamentation. The phenomenon that longer wavelengths have less plasma defocusing was observed.

Applications of filamentation in transparent solids for micro/nano-processing

The research on filamentation in solids had focused on the supercontinuum spectrum [11,91], which usually does not cause permanent modifications or damage due to the ultrafast laser peak intensity limitation. With the advancement of high peak power ultrafast laser technology, the energy deposition of ultrafast laser filamentation in solids can cause the refractive index change or permanent structural modification. It has attracted attention in the application fields such as micro-optical device manufacturing and material precision processing [12,92,93].

Filamentation-induced material modification processing

The primary foundation of the optical waveguide structure is the refractive index change and birefringence change in the filamentary traces of solids. Waveguiding is induced by positive refractive index changes, and negative refractive index changes cause a strong confinement mode [65,94,95].

The curved waveguide structures were created by Watanabe et al. [96] because the previous filamentary trace changes the refractive index of the surrounding solids, affecting subsequent filamentary propagation and bending the propagation path. The implementation of wavelength-divided 3-dimensional directional couplers is shown in Fig. 9A. Furthermore, multimode interference waveguides fabricated by fs laser filamentary traces in silica can split single-mode light into multimode light [97]. Tarasova et al. [98] used the filamentary traces in quartz glass to prepare geometric microchannels based on positive refractive index changes. When ultraviolet (UV)-detected light with a wavelength of 257 nm transfers through the geometric microchannel, the spatial intensity distribution changes along the geometric microchannels. The optical patterns of UV illumination are shown in Fig. 9B. In BK7 glass, Dharmadhikari et al. [99] described using a Bessel filamentation produced by an axicon lens to directly write waveguide structures with the lowest propagation loss of 0.19 dB/cm at 635 and 1,550 nm. The multimode optical fibers with 4-core structures made by Cho et al. [100] are depicted in Fig. 9C. By using plasma self-channeling induced by fs laser filamentation, refractive index change traces with diameters of 5 to 8 μm in an optical fiber were fabricated.

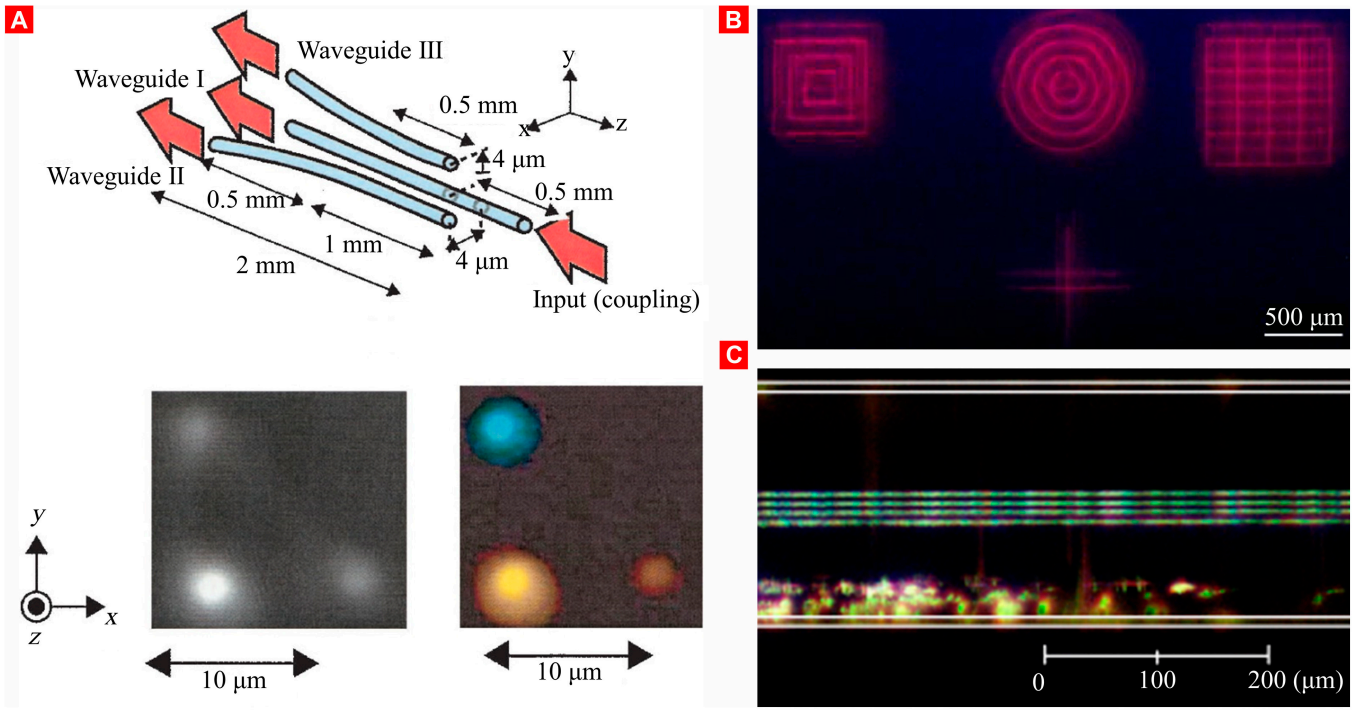

Fig. 9. (A) Schematic of the curved directional coupler and the output patterns of the coupler [96]. (B) Optical structures under UV illumination [98]. (C) Four-core structures in an optical fiber [100].

The filamentary traces can be used as a "fiber" to guide light beams and as a "fiber wall" to confine light beams. Through the refocusing mechanism of fs pulse filamentation, Chen and colleagues have created single/double layer waveguide structures in $LiTaO_3$ [101] and 6H-SiC [102] crystals. The beam can only transmit in the direction perpendicular to the modified trace because the modified traces exhibit the negative refractive index change. By changing the pulse energy, the number of refocusing in the material can be managed. Multilayer waveguide structures can be realized by spontaneously forming multiple focusing spots separated by a few micrometers shown in Fig. 10A. In Fig. 10B, Kroesen et al. [103] created the intricate 2-dimensional waveguide in $LiNbO_3$ using fs filamentary traces. In the c-band of communications, the complex structure shows narrowband reflection, symmetric guiding with high mode fidelity, and low loss. By using fs laser filamentation and a potassium tantalate niobate crystal, Liu and colleagues [104] created a hexagonal cladding waveguide. Particularly in their ferroelectric state, the filamentary traces tightly confined the polar nano-regions and increased waveguide birefringence, achieving outstanding polarization.

By embedding 3-dimensional filamentary traces in the transparent medium, the energy distribution and transmission mode of the light beam can be changed. In addition, it is possible to analyze external environment changes by wavelength shift, including temperature, contact force, pressure, and axial

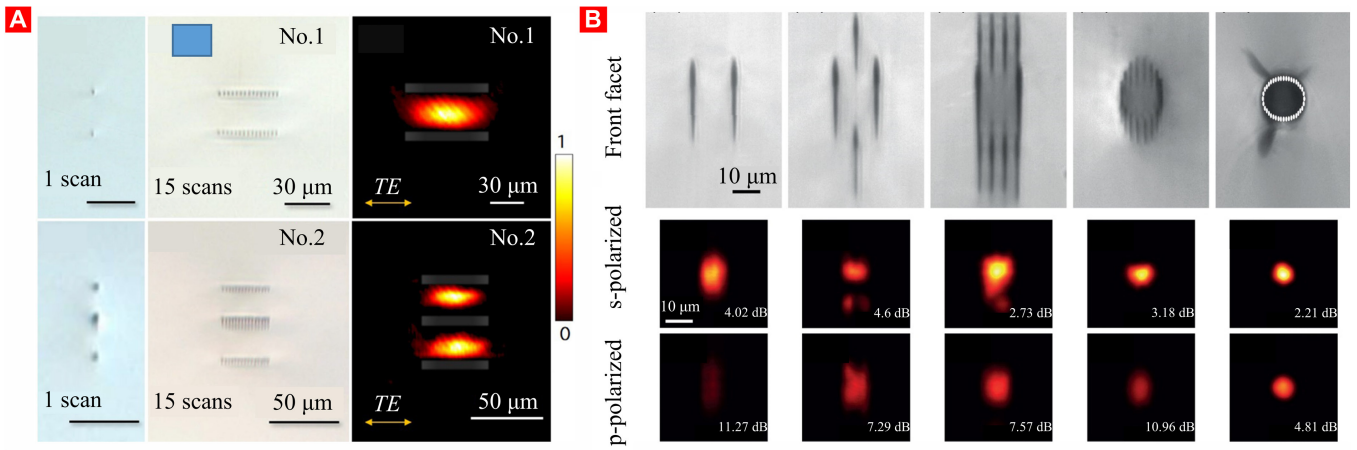

Fig. 10. (A) Characterizations of the horizontal polarization optical waveguides [101]. (B) Characterizations of the different 2-dimensional waveguide structures [103].

strain sensing. A 6 × 6 array of Dammann gratings with various thicknesses and layer counts in polished fused silica were created by Liebers et al. [105] using fs filamentary traces. All manufactured gratings exhibit strong birefringence index change and a maximum diffraction efficiency of 38.8%. By embedding fs laser filamentary traces into silica glass, Lee et al. [106] produced the 3-dimensional multilevel phase-type diffractive lenses. The maximum efficiency was 56.9% with a 4-level birefringence diffractive lens. A microfabrication method for vortex grating inside glass using fs filamentation was presented by Yamada et al. [107]. After reconstructing the vortex beam, it has the first-order diffraction efficiency of 19.6 at 632.8 nm. Ran and Qu [108] reported the fs filamentary trace array as refractive index gratings in fused silica. The maximum refractive index change was approximately 1.1×10^{-3}, and the highest diffraction efficiency was 10^{-4} for a 5 μm period grating. Gaižauskas et al. [109] fabricated the uniform filamentary trace array with azimuthal symmetry in a 9.3 μm fiber waveguide core diameter, generating strong fiber Bragg gratings with π-phase-shifted Bragg grating resonance with 25 pm bandwidth resonances in the telecommunication band.

Ertorer et al. [110] fabricated Bragg gratings with as low as 2.3% reflectivity using fs filamentary traces in sapphire fibers. Then, the wavelength-division-multiplexed Bragg grating arrays, including 5 groups with different pitches, were prepared in sapphire fiber. Bragg grating array can function at temperatures as high as 1,600 °C as a quasi-distributed high temperature sensor. By introducing filamentary traces into the cladding and core of the fiber, Xu et al. [111] produced the chirped Bragg gratings. The chirped filamentary geometry produced the narrowed radiation patterns that had 335 pm bandwidth resolved lines without the use of collimating or focusing optics, as shown in Fig. 11A and B. After that, they used fs laser filamentation to drill opening high-aspect ratio nano-holes in optical fiber [112]. Under the influence of capillary force, nematic liquid crystal was introduced into the cylindrical walls of the hollow filamentation grating. Cylindrical walls, nematic liquid crystal, and Bragg gratings combine to generate an extinction ratio of up to 20 dB at a band of 5 nm, with only a 1 dB insertion loss. Strong photonic stopbands can be formed inside the fiber by chemically etching the nanoholes. By saturating the nanoholes with solvents and oils, Bragg gratings had accurately resolved shifts for refractive index sensing from $n_H = 1$ to 1.67 [113]. A strongly contrasting azimuthal sensitivity was provided by the filamentary trace arrays inscribed in fiber with parallel and orthogonal direction off-axis, as shown in Fig. 11C and D [114].

For filamentation-induced material modification processing, the critical point of processing application is to improve the waveguide efficiency and the sensing sensitivity. The effect

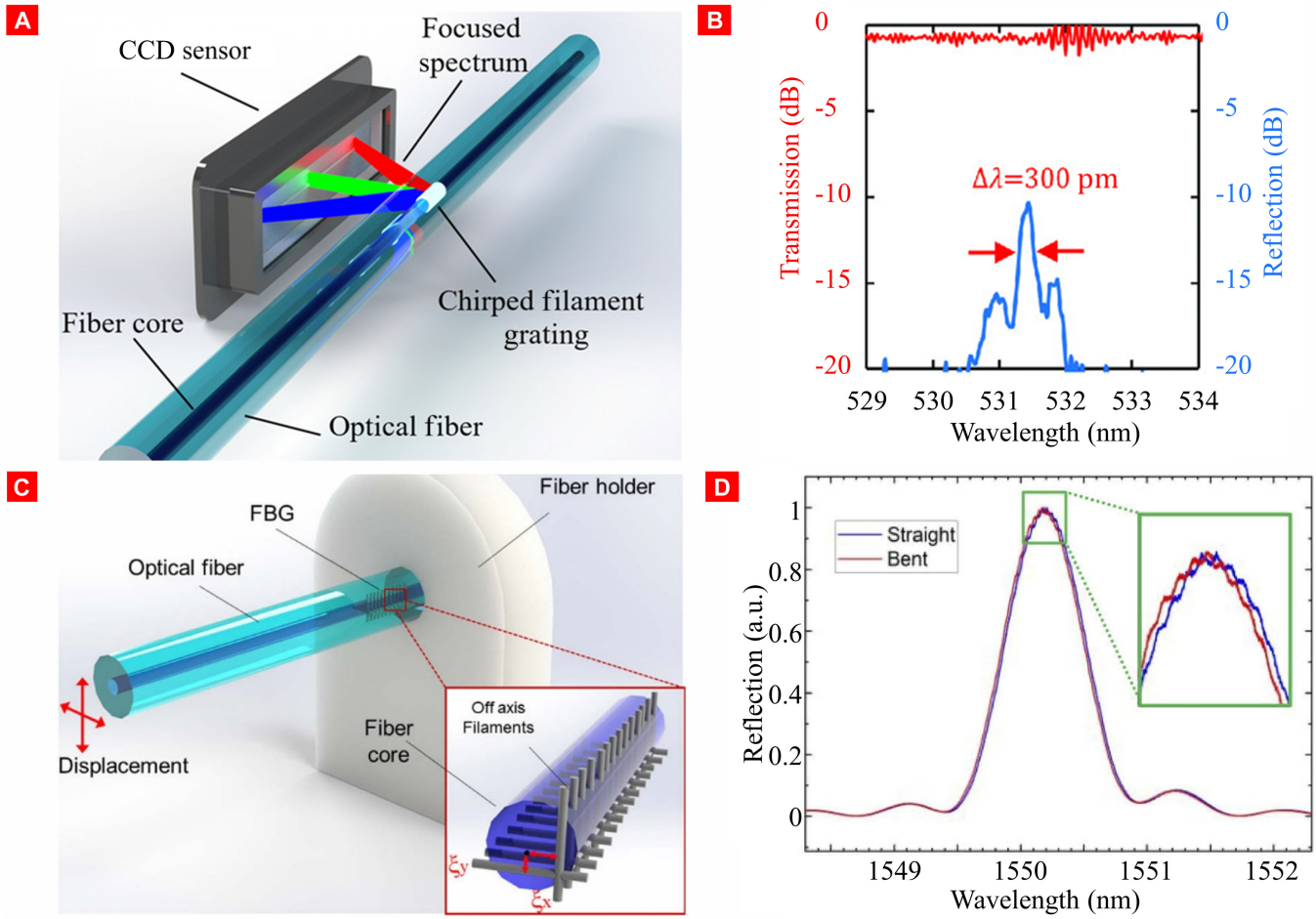

Fig 11. (A) Schematic of the chirped Bragg gratings. (B) Radiation patterns at 3 color light sources [111]. (C) Schematic of the Bragg grating with orthogonal filamentary traces. (D) Stress-induced wavelength shift [114].

of laser processing parameters on the refractive index and the effect of filamentation-induced modified arrays on the refractive index of materials need to be adjusted during the processing. Since filamentary traces are generated inside transparent solid materials, environmental factors tend to affect solid media with the potential to work in extreme environments or to analyze changes in the external environment. Conversely, the external environment can also impact waveguide efficiency, potentially leading to a reduction in laser intensity and displacement of the wavelength.

Filamentation-induced drilling and cutting

Increasing pulse energy will cause ultrafast laser filamentation to produce type III modification, including microcracks and voids in solids, to achieve high aspect ratio drilling and precision cutting.

Rahnama et al. [115] reported that a quartz microchannel was fabricated by fs laser filamentation. The initial diameter of microchannels in quartz glass is about 200 to 300 μm. Compared to the laser spot of 30 μm, the bottom diameter of the microchannel was reduced to 21 μm. Esser et al. [32] investigated ps laser filamentation drilling induced by a burst train in BK7 glass. Compared to the multiple pulse drilling (repetition rate, ~500 Hz), the burst trains can improve the glass ductility and cause the high-aspect ratio holes. Varel et al. [116] produced the void array with an aspect ratio of more than 200 and a diameter of 1 to 2 μm in poly L-lactide (PLLA) using fs laser filamentation. The PLLA polymer medical coronary stent was helically cut along the void array. To prevent the glass surfaces from suffering severe damage during the fs filamentation processing, Butkus et al. [117–119] created a series of void arrays along the processing path in glass samples covered with a water layer, as shown in Fig. 12A. A 36-angle sprocket cut in glass with a thickness of 1 mm by this technique is shown in Fig. 12B. A glass cleaving strategy based on the filamentation-induced void array was proposed by Butkus et al. [120]. A double-layer periodic void array was fabricated in glass by fs laser filamentation. The glass thickness of 700 μm was cleaved by applying external mechanical stress. Ahmed et al. [121] utilized the ps laser burst composed of sub-pulses with decreasing energy and a time interval of 24 ns to achieve filamentation-induced cleaving in soda-lime glass in Fig. 12C. Two types of microcracks were observed, with radial cracks forming the laser-affected zone by passing through the filamentary trace. Maximum roughness Rz along the 1.1 mm thick glass cross-section is about 4 μm, as shown in Fig. 12D. Werr et al. [122] generated the filamentary traces by burst trains and guided the cleaving of glass substrates. The cleaved surface had a root mean square roughness of 3 to 500 nm. Li et al. [123] first produced filamentary traces through the whole material inside the glass by ps laser. Then, they realized the automatic separation along the processing path by heating the modified traces with the CO_2 laser. In this way, anisotropic glass cutting can achieve a thickness of 0.7 mm and surface roughness $R_a = 0.5$ μm.

Based on the ps laser filamentation-induced phase change in sapphire, the chemical resistance of the filamentary traces decreases sharply [70]. Flat microchannels were obtained by chemical etching, as shown in Fig. 13A. Moreover, using ps laser filamentation and chemical etching, a high precision cutting surface with an 800 nm roughness (R_a) was produced. In Fig. 13B, the arbitrary cutting path can be achieved by this technique [124].

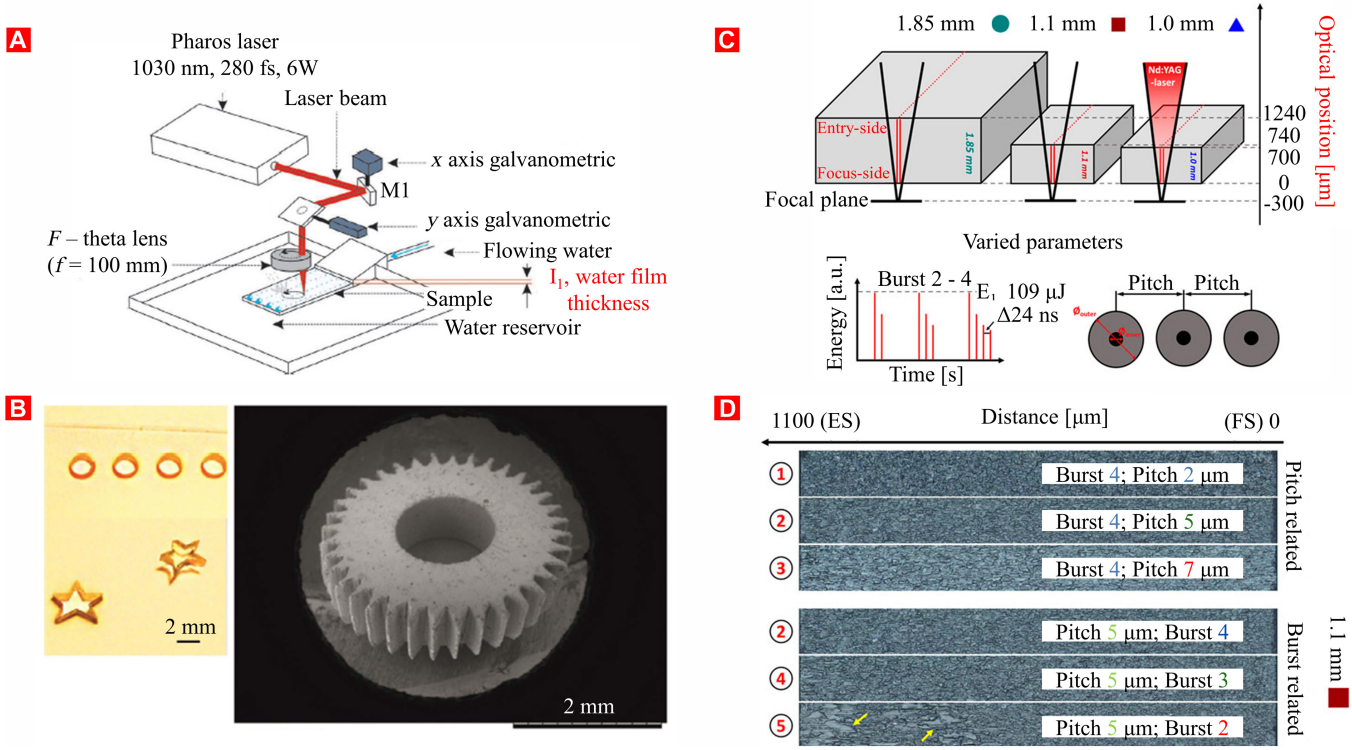

Fig. 12. (A) Experimental setup of filamentation-induced processing with a water layer. (B) Complex shape samples fabricated by filamentation [117]. (C) Schematic diagram of burst-mode filamentation-induced processing. (D) Morphology of the cutting surfaces by burst-mode filamentation [121].

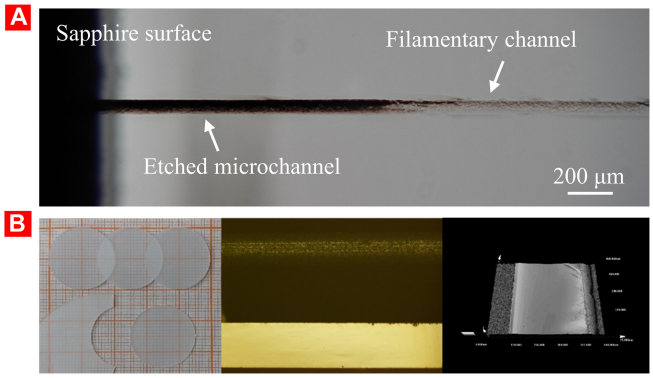

Fig.13. (A) Optical image of the etched filamentary microchannel [70]. (B) Sapphire samples processed by ps laser filamentation cutting (left), comparison on the optical micrograph between the edge surface of crude sapphire and cut surface of processed sapphire (middle), and the laser scanning confocal micrograph of cut surface of processed sapphire (right) [124].

For filamentation-induced drilling and cutting, control of crack extension is critical for processing applications. Filamentary propagation is beneficial for achieving large-depth drilling and large-thickness cutting of transparent materials. It often requires stress application and chemically assisted methods for drilling and cutting.

Filamentation-induced welding and joining

Ultrafast laser filamentation inevitably causes material melting due to the accumulation effect of multi-pulse incidence. This presents a novel technique for micro-welding/joining of transparent materials.

The schematic representation of the ultrafast laser filamentation-induced welding method is shown in Fig. 14A [125]. The ultrafast laser is focused near the interface of transparent materials to create a filamentation. The materials close to the filamentation are melted by the energy deposited. The initial space between the 2 materials is filled by the melted substance. The re-solidification process enables the welding of transparent materials without the intermediary layer [126].

The capability of fs laser filamentation to weld transparent materials was demonstrated by Tamaki et al. [127]. The filamentary traces with a length of 30 μm bridged the glass samples. They pointed out that the glass substrates were successfully welded when the gap between the materials was narrower than $\lambda/4$. Subsequently, Chen et al. [128] investigated the ability of ps laser filamentation welding to fill micrometer-scale gaps. With a preexisting gap of 3 μm, 2 glasses were successfully

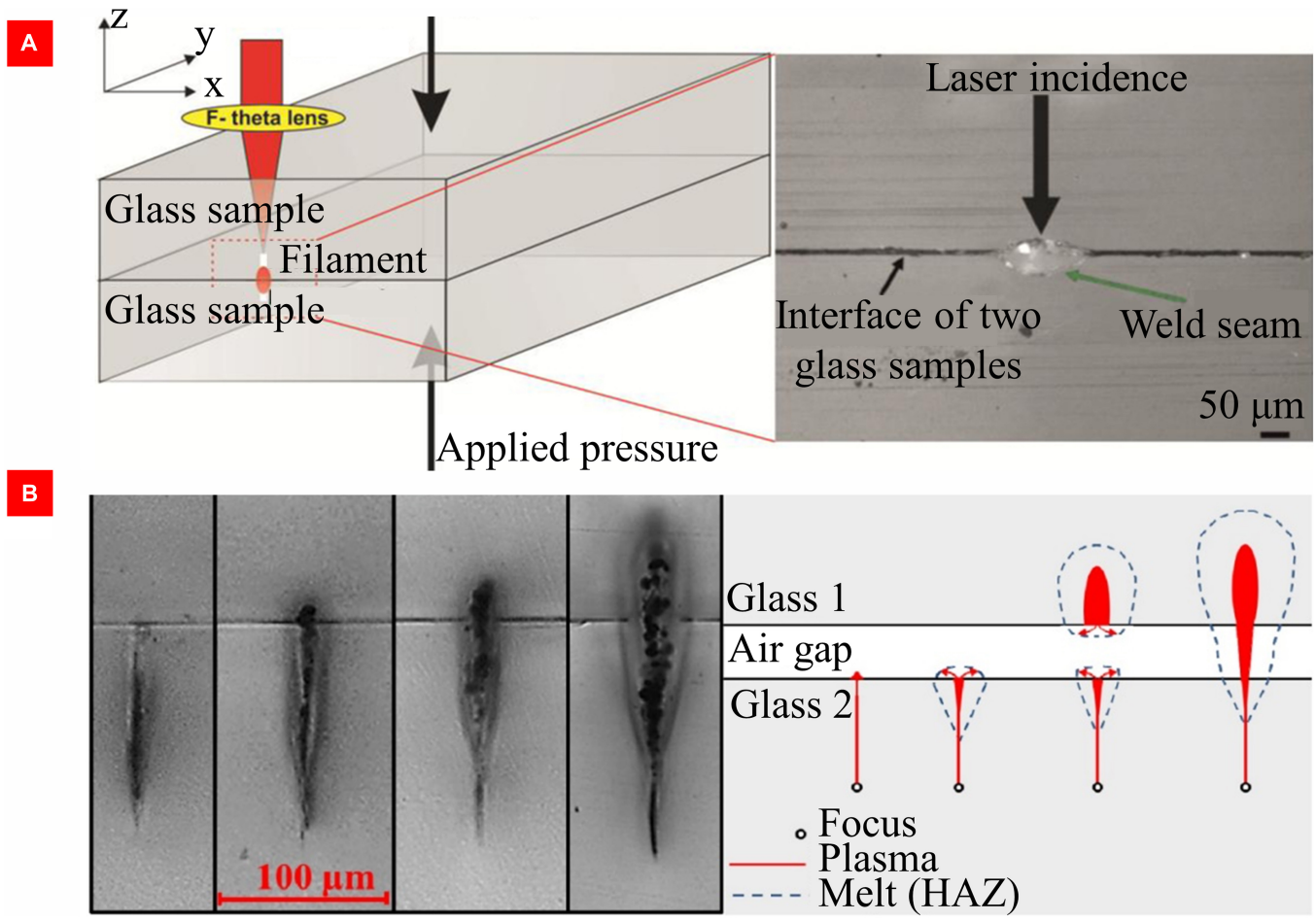

Fig.14. (A) Schematic diagram of filamentation welding and actual weld seam [125]. (B) Cross-sections of different welding patterns at different focal positions and illustration of mechanism [128].

welded. As shown in Fig. 14B, the gap that can be welded is strongly dependent on the filamentation position relative to the interface. Zhang et al. [129] reported that glass–glass welding samples with excellent optical transmission and sealing effectiveness were created by 1,064 nm ps laser filamentation. High-strength welds (30 MPa) can be produced with a smooth microstructure when the air gap is 2 μm. For welding of dissimilar materials, direct micro-welding between glass and copper substrates was demonstrated by Ozeki et al. [130] using fs laser filamentation. The strength of the joints can reach >16 MPa. Using nondiffractive fs laser Bessel filamentation, Cheng and colleagues [131] achieved the large-focal-depth welding between the glass and silicon. The sample has a shear joining strength that can reach 16.5 MPa. Chambonneau et al. [132] recently welded the silicon and copper using ps laser filamentation by pre-compensating the nonlinear focal shift in silicon. The pre-compensation of the focal shift achieved a shear joining strength of 2.2 MPa.

For filamentation-induced welding and joining, the critical point of application is sealing and connection strength. Filamentation-induced welding has the advantage of welding dissimilar materials, but the welding effect zone is large, which tends to reduce the quality of the media around the welding zone.

For ultrafast laser filamentation-induced micro/nano-processing, GaN layer separation from sapphire substrates by burst-mode filamentation was studied by Ji and colleagues [33]. The separated interface can be made flat and smooth using burst-mode filamentation. It offers a novel application for ultrafast laser filamentation-induced micro/nano-processing in solids.

Conclusions and Perspective

Toward ultrafast laser filamentation for solid micro/nano-processing, we have mainly reviewed recent research advances of filamentation induced by ultrafast laser in solids from primary filamentation characteristics, and modulations, filamentary propagation models to the representative filamentation-induced micro and nano-processing in solids. According to the exotic characteristics of long distance propagation and background energy reservoir of filamentation in transparent media, the latest methods of modulating filamentary propagation and adjusting filamentary plasma in transparent media, including the spatial shaping of the pulse profile and the temporal modulation of the pulse burst, are introduced. Three modification types of transparent media induced by ultrafast laser filamentation are introduced to provide a basis for ultrafast laser filamentation-induced micro- and nano-processing. Filamentation-induced micro- and nano-processing applications in solid media are presented according to different material modification types. Ultrafast laser filamentation provides new opportunities for micro- and nano-processing, including waveguiding, sensing, drilling, cutting, and welding.

There remain opportunities and challenges from principle to application toward the filamentation-induced micro- and nano-processing. First, the output modes of multiple pulses and pulse bursts are increasingly used in ultrafast laser filamentation-induced processing. In the case of multiple pulse or sub-pulse inputs, how the modified material and the plasma induced by the previous pulse affect the nonlinear propagation of subsequent pulses needs further explanation. Although the filamentation propagation distance and filamentation position have been effectively modulated, the homogeneity of material modification type and the uniformity of filamentary traces need to be further controlled because the precision of micro- and nano-processing depends heavily on the material modification type and the morphology of the filamentary trace. In addition to the spatiotemporal modulation of laser pulses, preliminary results have been obtained for the study of applying external electric and magnetic fields to regulate plasma morphology and density. Since the essence of filamentation is a plasma channel, this may be one of the methods to modulate filamentary propagation in transparent media by external conditions. The region around the filamentary traces with mild residual tensions and minor modifications is also one of the critical points in developing ultrafast laser filamentation-induced processing in solids. One-step fabrication into filamentary trace arrays by microlens arrays would be one of the methods to fabricate precise filamentary trace arrays, which contributes to processing accuracy and sensing precision and improves processing efficiency. It should be noted that due to the high density of the filamentary plasma, high pressure shock waves cannot be neglected in the filamentary propagation. How to utilize the high pressure shock waves induced by filamentary plasma remains to be confirmed, which may lead to new micro- and nano-processing methods, such as separating materials by shock waves for macroscopic transfer of light-emitting diodes.

Acknowledgments

Funding: This work was supported by the National Natural Science Foundation of China (no. 51975017), the National Key R&D Program of China (no. 2018YFB1107500), and the Scientific Research Project of Beijing Educational Committee (no. KZ202110005012). **Author contributions:** T.Y. investigated the literature and wrote the manuscript. L.J. reviewed the final manuscript. **Competing interests:** The authors declare that they have no known competing financial interests or personal relationships that could have appeared to influence the work reported in this paper.

References

1. Braun A, Korn G, Liu X, Du D, Squier J, Mourou G. Self-channeling of high-peak-power femtosecond laser pulses in air. *Opt Lett*. 1995;20(1):Article 73.
2. Chin SL, Wang T-J, Marceau C, Wu J, Liu JS, Kosareva O, Panov N, Chen YP, Daigle J-F, Yuan S, et al. Advances in intense femtosecond laser filamentation in air. *Laser Phys*. 2012;22(1):1–53.
3. Couairon A, Mysyrowicz A. Femtosecond filamentation in transparent media. *Phys Rep*. 2007;441(2-4):47–189.
4. Hercher M. Laser induced damage in transparent media. *J Opt Soc Am*. 1964;54:Article 563.
5. Strickland D, Mourou G. Compression of amplified chirped optical pulses. *Opt Commun*. 1985;56(3):219–221.
6. Kandidov VP, Shlenov SA, Kosareva OG. Filamentation of high-power femtosecond laser radiation. *Quant Electron*. 2009;39(3):205–228.
7. Chin SL, Hosseini SA, Liu W, Luo Q, Théberge F, Aközbek N, Becker A, Kandidov VP, Kosareva OG, Schroeder H. The

propagation of powerful femtosecond laser pulses in optical media: Physics, applications, and new challenges. *Can J Phys*. 2005;83(9):863–905.
8. Kasparian J, Wolf J-P. Physics and applications of atmospheric nonlinear optics and filamentation. *Opt Express*. 2008;16(1):Article 466.
9. Geints YE, Zemlyanov AA. Dynamics of femtosecond synthesized coronary profile laser beam filamentation in air. *J Optic*. 2021;23(10):1–53.
10. Papazoglou DG, Abdollahpour D, Tzortzakis S. Ultrafast electron and material dynamics following femtosecond filamentation induced excitation of transparent solids. *Appl Phys Mater Sci Process*. 2014;114(1):161–168.
11. Liu W, Petit S, Becker A, Aközbek N, Bowden CM, Chin SL. Intensity clamping of a femtosecond laser pulse in condensed matter. *Opt Commun*. 2002;202(1-3):189–197.
12. Watanabe W, Tamaki T, Ozeki Y, Itoh K. *Filamentation in ultrafast laser material processing*. Berlin, Heidelberg: Springer; 2011.
13. Kasparian J, Sauerbrey R, Chin SL. The critical laser intensity of self-guided light filaments in air. *Appl Phys B Lasers Opt*. 2000;71(6):877–879.
14. Liu WW. Intensity clamping during femtosecond laser filamentation. *Chin J Phys*. 2014;52(1):465–489.
15. Amina JL, Yan T, Wang Y, Li L. Characteristics of 1064nm picosecond laser induced filamentary tracks and damages in sapphire. *Opt Laser Technol*. 2019;116:232–238.
16. Marburger JH. Self-focusing: Theory. *Progress Quant Electron*. 1975;4:35–110.
17. Galinis J, Tamošauskas G, GraŽulevičiute I, Keblyte E, Jukna V, Dubietis A. Filamentation and supercontinuum generation in solid-state dielectric media with picosecond laser pulses. *Phys Rev A - Atom Mol Optic Phys*. 2015;92(3):Article 033857.
18. Dai Y, Patel A, Song J, Beresna M, Kazansky PG. Void-nanograting transition by ultrashort laser pulse irradiation in silica glass. *Opt Express*. 2016;24(17):Article 19344.
19. Poumellec B, Lancry M, Chahid-Erraji A, Kazansky PG. Modification thresholds in femtosecond laser processing of pure silica: Review of dependencies on laser parameters invited. *Optic Mater Express*. 2011;1(4):Article 766.
20. Isaacs J, Hafizi B, Johnson LA, Rosenthal EW, Mrini L, Peñano J. Modeling the propagation of a high-average-power train of ultrashort laser pulses. *Opt Express*. 2022;30(13):Article 22306.
21. Couairon A, Bergé L. Light filaments in air for ultraviolet and infrared wavelengths. *Phys Rev Lett*. 2002;88(13):4.
22. Papazoglou DG, Zergioti I, Tzortzakis S, Sgouros G, Maravelias G, Christopoulos S, Fotakis C. Sub-picosecond ultraviolet laser filamentation-induced bulk modifications in fused silica. *Appl Phys Mater Sci Process*. 2005;81(2):241–244.
23. Sowa S, Watanabe W, Nishii J, Itoh K. Filamentary cavity formation in poly(methyl methacrylate) by single femtosecond pulse. *Appl Phys Mater Sci Process*. 2005;81(8):1587–1590.
24. Gražulevičiūtė I, Skeivytė M, Keblytė E, Galinis J, Tamošauskas G, Dubietis A. Supercontinuum generation in YAG and sapphire with picosecond laser pulses. *Lith J Phys*. 2015;55(2):110–116.
25. Apeksimov DV, Golik SS, Zemlyanov AA, Kabanov AM, Mayor AY, Petrov AV. Dynamics of the structure of multiple filamentation domain of laser pulses in glass. *Atmos Ocean Optic*. 2017;30(3):222–225.
26. Nguyen NT, Saliminia A, Liu W, Chin SL, Vallée R. Optical breakdown versus filamentation in fused silica by use of femtosecond infrared laser pulses. *Opt Lett*. 2003;28(17):Article 1591.
27. Feigenbaum E, Laurence TA. Filament damage formation in fused silica glass as a result of 1–50 ps near-infrared laser pulses. *Appl Opt*. 2017;56(13):Article 3666.
28. Dharmadhikari JA, Deshpande RA, Nath A, Dota K, Mathur D, Dharmadhikari AK. Effect of group velocity dispersion on supercontinuum generation and filamentation in transparent solids. *Appl Phys B Lasers Opt*. 2014;117(1):471–479.
29. Moll KD, Gaeta AL. Role of dispersion in multiple-collapse dynamics. *Opt Lett*. 2004;29(9):Article 995.
30. Paipulas D, Balskiene A, Sirsutkaitis V. Experimental study of filamentation and supercontinuum generation in laser-modified fused silica. *Lith J Phys*. 2012;52(4):327–333.
31. Javaux Léger C, Mishchik K, Dematteo-Caulier O, Skupin S, Chimier B, Duchateau G, Bourgeade A, Hönninger C, Mottay E, Lopez J, et al. Effects of burst mode on transparent materials processing. *Laser-Based Micro- Nanoprocess IX*. 2015;9351:132–141.
32. Esser D, Rezaei S, Li J, Herman PR, Gottmann J. Time dynamics of burst-train filamentation assisted femtosecond laser machining in glasses. *Opt Express*. 2011;19(25):Article 25632.
33. Sun W, Sun W-g, Yan T-y, Wang Y-h, Ji L-f. Spatiotemporal evolution of high-aspect-ratio filamentary trace in sapphire of picosecond pulse burst-mode for laser lift-off. *J Cent South Univ*. 2022;29(10):3304–3311.
34. Ma R, Ji L, Yan T, Zhang L, Zhang T. Influence of ambient gases on plasma dynamics of ultrafast laser-induced filamentation in sapphires. *Opt Express*. 2020;28(14):Article 20461.
35. Liu W, Théberge F, Arévalo E, Gravel J-F, Becker A, Chin SL. Experiment and simulations on the energy reservoir effect in femtosecond light filaments. *Opt Lett*. 2005;30(19):Article 2602.
36. Liu W, Gravel JF, Théberge F, Becker A, Chin SL. Background reservoir: Its crucial role for long-distance propagation of femtosecond laser pulses in air. *Appl Phys B Lasers Opt*. 2005;80(7):857–860.
37. Apeksimov DV, Golik SS, Zemlyanov AA, Iglakova AN, Kabanov AM, Kuchinskaya OI, Matvienko GG, Oshlakov VK, Petrov AV, Sokolova EB. Multiple filamentation of collimated laser radiation in water and glass. *Atmos Ocean Optic*. 2016;29(2):135–140.
38. Geints YE, Golik SS, Zemlyanov AA, Kabanov AM, Petrov AV. Microstructure of the multiple-filamentation zone formed by femtosecond laser radiation in a solid dielectric. *Quant Electron*. 2016;46(2):133–141.
39. Wang J, Guo Y, Song X, Lin J. Flexible manipulation of the onset and terminal positions of femtosecond laser filamentation in fused silica via controlling beam profile before axicon. *Opt Commun*. 2022;516:Article 128262.
40. Lü J-Q, Li P-P, Wang D, Tu C, Li Y, Wang H-T. Extending optical filaments with phase-nested laser beams. *Photo Res*. 2018;6(12):Article 1130.
41. Li J, Tan W, Si J, Tang S, Kang Z, Hou X. Control of the spatial characteristics of femtosecond laser filamentation in glass via feedback-based wavefront shaping with an annular phase mask. *Opt Express*. 2021;29(4):Article 5972.

42. Camino A, Hao Z, Liu X, Lin J. Control of laser filamentation in fused silica by a periodic microlens array. *Opt Express*. 2013;21(7):Article 7908.
43. Majus D, Jukna V, Valiulis G, Dubietis A. Generation of periodic filament arrays by self-focusing of highly elliptical ultrashort pulsed laser beams. *Phys Rev A - Atomic, Mol Optic Phys*. 2009;79(3):Article 033843.
44. Li D, Xi T, Zhang L, Tao H, Gao X, Lin J, Hao Z. Interference-induced filament array in fused silica. *Opt Express*. 2017;25(20):Article 23910.
45. Wang J, Guo Y, Song X, Guo K, Lin J. Multi-dimensional control of femtosecond laser filaments by inserting a wedge plate in the forced focusing region. *Phys Plasma*. 2022;29(1):Article 012301.
46. Li D, Chang J, Xu L, Zhang L, Xi T, Hao Z. Free control of filaments rotating induced by vortex femtosecond laser beams interference in fused silica. *Opt Laser Technol*. 2022;150:Article 107974.
47. Wang J, Guo Y, Song X, Lin J. Manipulation of femtosecond laser multi-filament array by spatiotemporal phase modulation. *Opt Commun*. 2021;495:Article 127113.
48. Bérubé J-P, Vallée R, Bernier M, Kosareva O, Panov N, Kandidov V, Chin SL. Self and forced periodic arrangement of multiple filaments in glass. *Opt Express*. 2010;18(3):Article 1801.
49. Li PP, Cai MQ, Lü JQ, Wang D, Liu GG, Qian SX, Li Y, Tu C, Wang HT. Control of femtosecond multi-filamentation in glass by designable patterned optical fields. *AIP Adv*. 2016;6(12):Article 125103.
50. Li D, Chang J, Xi T, Li D, Ji L, Liang W, Hao Z, Zhang L. Filament-necklace generated by femtosecond vector beams in fused silica. *Opt Commun*. 2022;2023(533):Article 129283.
51. Lin Z, Hong M. Femtosecond laser precision engineering: From micron, submicron, to nanoscale. *Ultraf Sci*. 2021;2021:Article 9783514.
52. Ams M, Marshall GD, Dekker P, Dubov M, Mezentsev VK, Bennion I, Withford MJ. Investigation of ultrafast laser-photonic material interactions: Challenges for directly written glass photonics. *IEEE J Select Topic Quant Electron*. 2008;14(5):1370–1388.
53. Gamaly EG, Rode AV. Physics of ultra-short laser interaction with matter: From phonon excitation to ultimate transformations. *Progress Quant Electron*. 2013;37(5): 215–323.
54. Houard A, Jukna V, Point G, André Y-B, Klingebiel S, Schultze M, Michel K, Metzger T, Mysyrowicz A. Study of filamentation with a high power high repetition rate ps laser at 103 μm. *Opt Express*. 2016;24(7):Article 7437.
55. Onda S, Watanabe W, Yamada K, Itoh K, Nishii J. Study of filamentary damage in synthesized silica induced by chirped femtosecond laser pulses. *J Opt Soc Am B*. 2005;22(11):Article 2437.
56. Sudrie L, Franco M, Prade B, Mysyrowicz A. Study of damage in fused silica induced by ultra-short IR laser pulses. *Opt Commun*. 2001;191(3-6):333–339.
57. Sudrie L, Couairon A, Franco M, Lamouroux B, Prade B, Tzortzakis S, Mysyrowicz A. Femtosecond laser-induced damage and filamentary propagation in fused silica. *Phys Rev Lett*. 2002;89(18):Article 186601.
58. Couairon A, Sudrie L, Franco M, Prade B, Mysyrowicz A. Filamentation and damage in fused silica induced by tightly focused femtosecond laser pulses. *Phys Rev B - Condens Matter Mater Phys*. 2005;71(12):Article 125435.
59. Will M, Nolte S, Chichkov BN, Tünnermann A. Optical properties of waveguides fabricated in fused silica by femtosecond laser pulses. *Appl Opt*. 2002;41(21):Article 4360.
60. Poumellec B, Lancry M. Damage thresholds in femtosecond laser processing of silica: A review. Paper presented at: Optics InfoBase Conference Papers. 2010.
61. Shimotsuma Y, Kazansky PG, Qiu J, Hirao K. Self-organized nanogratings in glass irradiated by ultrashort light pulses. *Phys Rev Lett*. 2003;91(24):Article 247405.
62. Ashkenasi D, Müller G, Rosenfeld A, Stoian R, Hertel IV, Bulgakova NM, Campbell EEB. Fundamentals and advantages of ultrafast micro-structuring of transparent materials. *Appl Phys Mater Sci Process*. 2003;77(2):223–228.
63. Schaffer CB, Jamison AO, Mazur E. Morphology of femtosecond laser-induced structural changes in bulk transparent materials. *Appl Phys Lett*. 2004;84(9):1441–1443.
64. Benayas A, Jaque D, McMillen B, Chen KP. Thermal stability of microstructural and optical modifications induced in sapphire by ultrafast laser filamentation. *J Appl Phys*. 2010;107(3):Article 033522.
65. Zhang B, Wang L, Chen F. Recent advances in femtosecond laser processing of LiNbO3 crystals for photonic applications. *Laser Photo Rev*. 2020;14(8):Article 1900407.
66. Ródenas A, Torchia GA, Lifante G, Cantelar E, Lamela J, Jaque F, Roso L, Jaque D. Refractive index change mechanisms in femtosecond laser written ceramic Nd:YAG waveguides: Micro-spectroscopy experiments and beam propagation calculations. *Appl Phys B Lasers Opt*. 2009;95(1):85–96.
67. Burghoff J, Hartung H, Nolte S, Tünnermann A. Structural properties of femtosecond laser-induced modifications in LiNbO3. *Appl Phys Mater Sci Process*. 2007;86(2):165–170.
68. Paipulas D, Kudriašov V, Malinauskas M, Smilgevĭcius V, Sirutkaitis V. Diffraction grating fabrication in lithium niobate and KDP crystals with femtosecond laser pulses. *Appl Phys Mater Sci Process*. 2011;104(3):769–773.
69. Papazoglou DG, Tzortzakis S. Physical mechanisms of fused silica restructuring and densification after femtosecond laser excitation invited. *Optic Mater Express*. 2011;1(4): Article 625.
70. Hernandez-Rueda J, Clarijs J, Van Oosten D, Krol DM. The influence of femtosecond laser wavelength on waveguide fabrication inside fused silica. *Appl Phys Lett*. 2017;110(16):Article 161109.
71. Yan T, Ji L, Ma R, Amina LZ, Lin Z. Modification characteristics of filamentary traces induced by loosely focused picosecond laser in sapphire. *Ceram Int*. 2020;46(10):16074–16079.
72. Jing C, Qi X, Wang Z, Ma B, Ding C. Comparative study of femtosecond filamentation properties in the classical model and the full model for different incident pulse durations. *J Optic*. 2019;21(6):Article 065503.
73. Dorr MR, Garaizar FX, Hittinger JAF. Simulation of laser plasma filamentation using adaptive mesh refinement. *J Comput Phys*. 2002;177(2):233–263.
74. Couairon A, Brambilla E, Corti T, Majus D, de O, Kolesik M. Practitioner's guide to laser pulse propagation models and simulation. *Europe Phys J: Special Topic*. 2011;199(1):5–76.
75. Wang C, Zhao Q, Qian J, Li Y, Wang G, Zhang Y, Pan H, Bao Z, Bai F, Fan W. Propagation of focused ultrashort pulse laser during micromachining of sapphire. Paper presented at: Pacific Rim Laser Damage 2015: Optical Materials for High-Power Lasers. 2015.

76. Capuano L, de Zeeuw D, Römer GRBE. Towards a numerical model of picosecond laser-material interaction in bulk sapphire. *J Laser Micro Nanoeng*. 2018;13(3):166–177.
77. Sudrie L, Tzortzakis S, Franco M, Prade B, Mysyrowicz A, Couairon A, Bergé L. Self-guided propagation of ultrashort IR laser pulses in fused silica. *Phys Rev Lett*. 2001;87(21):Article 213902.
78. Blonskyi I, Kadan V, Shynkarenko Y, Yarusevych O, Korenyuk P, Puzikov V, Grin' L. Periodic femtosecond filamentation in birefringent media. *Appl Phys B Lasers Opt*. 2015;120(4):705–710.
79. Yan T, Ji L, Sun W. Characteristics and formation mechanism of filamentary plasma string induced by single picosecond laser pulse in sapphire. *Appl Phys Mater Sci Process*. 2022;128(1):1–8.
80. Brodeur A, Chien CY, Ilkov FA, Chin SL, Kosareva OG, Kandidov VP. Moving focus in the propagation of ultrashort laser pulses in air. *Opt Lett*. 1997;22(5):Article 304.
81. Sun Q, Jiang H, Liu Y, Zhou Y, Yang H, Gong Q. Effect of spherical aberration on the propagation of a tightly focused femtosecond laser pulse inside fused silica. *J Opt A Pure Appl Opt*. 2005;7(11):655–659.
82. Wu Z, Jiang H, Yang H, Gong Q. The refocusing behaviour of a focused femtosecond laser pulse in fused silica. *J Opt A Pure Appl Opt*. 2003;5(2):102–107.
83. Wu Z, Jiang H, Luo L, Guo H, Yang H, Gong Q. Multiple foci and a long filament observed with focused femtosecond pulse propagation in fused silica. *Opt Lett*. 2002;27(6):Article 448.
84. Wu Z, Jiang H, Sun Q, Yang H, Gong Q. Filamentation and temporal reshaping of a femtosecond pulse in fused silica. *Phys Rev A - Atom Mol Optic Phys*. 2003;68(6):8.
85. Mlejnek M, Wright EM, Moloney JV. Dynamic spatial replenishment of femtosecond pulses propagating in air. *Opt Lett*. 1998;23(5):382–384.
86. Martynovich EF, Dresviansky VP, Kuznetsov AV, Kuzakov AS, Popov AA, Alekseev SV, Losev VF, Ratakhin AN, Bagayev SN. Simulation of filamentation of single femtosecond laser pulses in LiF. *Laser Phys*. 2014;24(7):Article 074001.
87. Skupin S, Nuter R, Bergé L. Optical femtosecond filaments in condensed media. *Phys Rev A*. 2006;74(4):Article 043813.
88. Lim K, Durand M, Baudelet M, Richardson M. Transition from linear-to nonlinear-focusing regime in filamentation. *Sci Rep*. 2014;4(1):7217.
89. Amina, Ji LF, Yan TY, Ma R. Ionization behavior and dynamics of picosecond laser filamentation in sapphire. *Opto-Electron Adv*. 2019;2(8):Article 190003.
90. Nagar GC, Dempsey D, Shim B. Wavelength scaling of electron collision time in plasma for strong field laser-matter interactions in solids. *Commun Phys*. 2021;4(1):Article 96.
91. Jukna V, Galinis J, Tamosauskas G, Majus D, Dubietis A. Infrared extension of femtosecond supercontinuum generated by filamentation in solid-state media. *Appl Phys B Lasers Opt*. 2014;116(2):477–483.
92. Chin SL, Théberge F, Liu W. Filamentation nonlinear optics. *Appl Phys B Lasers Opt*. 2007;86(3):477–483.
93. Watanabe W, Tamaki T, Itoh K. Filamentation in laser microprocessing and microwelding. *Proc SPIE*. 2007;6733:Article 67332F.
94. Ródenas A, Maestro LM, Ramírez MO, Torchia GA, Roso L, Chen F, Jaque D. Anisotropic lattice changes in femtosecond laser inscribed Nd^{3+}:MgO: $LiNbO_3$ optical waveguides. *J Appl Phys*. 2009;106(1):Article 013110.
95. Saliminia A, Vallée R, Chin SL. Waveguide writing in silica glass with femtosecond pulses from an optical parametric amplifier at 1.5 μm. *Opt Commun*. 2005;256(4-6):422–427.
96. Watanabe W, Asano T, Yamada K, Itoh K, Nishii J. Wavelength division with three-dimensional couplers fabricated by filamentation of femtosecond laser pulses. *Opt Lett*. 2003;28(24):2491.
97. Watanabe W, Note Y, Itoh K. Fabrication of multimode interference waveguides in glass by use of a femtosecond laser. *Opt Lett*. 2005;30(21):2888.
98. Tarasova MA, Khorkov KS, Kochuev DA, Ivaschenko AV, Prokoshev VG. Formation of channels with changed refractive index at the filamentation of femtosecond laser radiation in quartz glass. *J Phys Conf Ser*. 2019;1164(1):Article 012023.
99. Dharmadhikari JA, Bernard R, Bhatnagar AK, Mathur D, Dharmadhikari AK. Axicon-based writing of waveguides in BK7 glass. *Opt Lett*. 2013;38(2):172.
100. Cho S-H, Kumagai H, Midorikawa K. Fabrication of multi-core structures in an optical fiber using plasma self-channeling. *Opt Express*. 2003;11(15):1780.
101. Li L, Nie W, Li Z, Zhang B, Wang L, Haro-Gonzalez P, Jaque D, Vazquez De Aldana JR, Chen F. Femtosecond laser writing of optical waveguides by self-induced multiple refocusing in LiTaO3 crystal. *J Lightwave Technol*. 2019;37(14):3452–3458.
102. Zhang B, He S, Yang Q, Liu H, Wang L, Chen F. Femtosecond laser modification of 6H–SiC crystals for waveguide devices. *Appl Phys Lett*. 2020;116(11):Article 111903.
103. Kroesen S, Horn W, Imbrock J, Denz C. Electro–optical tunable waveguide embedded multiscan Bragg gratings in lithium niobate by direct femtosecond laser writing. *Opt Express*. 2014;22(19):23339.
104. Wu P, Jiang X, Zhang B, He S, Yang Q, Li X, Ren Y, Chen F, Liu H. Mode-controllable waveguide fabricated by laser-induced phase transition in KTN. *Opt Express*. 2020;28(17):25633.
105. Liebers R, Mauer C, Nissel J, Jotz M, Wagner F. Waveguides in AR devices: Optimized cutting processes for transparent materials with laser technology. *Proc SPIE*. 2022;11988:Article 1198805.
106. Lee S, Nikumb S. Characteristics of filament induced Dammann gratings fabricated using femtosecond laser. *Opt Laser Technol*. 2007;39(7):1328–1333.
107. Yamada K, Watanabe W, Li Y, Itoh K, Nishii J. Multilevel phase-type diffractive lenses in silica glass induced by filamentation of femtosecond laser pulses. *Opt Lett*. 2004;29(16):1846.
108. Ran L, Qu S. Self-assembled volume vortex grating induced by femtosecond laser pulses in glass. *Curr Appl Phys*. 2009;9(6):1210–1212.
109. Gaižauskas E, Kudriašov V, Vaičaitis V, Sirutkaitis V. Fabrication of the refractive index gratings in optical glasses by the filamentary propagation of femtosecond laser pulses. *Proc SPIE*. 2006;6403:Article 640303.
110. Ertorer E, Haque M, Li J, Herman PR. Femtosecond laser filaments for rapid and flexible writing of fiber Bragg grating. *Opt Express*. 2018;26(7):9323.
111. Xu X, He J, He J, Xu B, Chen R, Wang Y, Yang Y, Wang Y. Efficient point-by-point Bragg grating inscription in sapphire fiber using femtosecond laser filaments. *Opt Lett*. 2021;46(11):2742.

112. Rahnama A, Mahmoud Aghdami K, Kim YH, Herman PR. Ultracompact lens-less "spectrometer in fiber" based on chirped filament-array gratings. *Adv Photon Res*. 2020;1(2):Article 2000026.
113. Rahnama A, Dadalyan T, Mahmoud Aghdami K, Galstian T, Herman PR. In-fiber switchable polarization filter based on liquid crystal filled hollow-filament Bragg gratings. *Adv Opt Mater*. 2021;9(19):2100054.
114. Mahmoud Aghdami K, Rahnama A, Ertorer E, Herman PR. Laser nano-filament explosion for enabling open-grating sensing in optical fibre. *Nat Commun*. 2021;12(1):6344.
115. Rahnama A, Mahlooji H, Djogo G, Azhari F, Herman PR. Filament-arrayed Bragg gratings for azimuthally resolved displacement sensing in single-mode fibers. *Opt Express*. 2022;30(3):4189.
116. Varel H, Ashkenasi D, Rosenfeld A, Wähmer M, Campbell EEB. Micromachining of quartz with ultrashort laser pulses. *Appl Phys Mater Sci Process*. 1997;65(4-5):367–373.
117. Vartapetov SK, Ganin DV, Lapshin KE, Obidin AZ. Femtosecond-laser fabrication of cyclic structures in the bulk of transparent dielectrics. *Quantum Elec*. 2015;45(8):725–730.
118. Butkus S, Paipulas D, Sirutkaitis R, Gaižauskas E, Sirutkaitis V. Rapid cutting and drilling of transparent materials via femtosecond laser filamentation. *J Laser Micro Nanoeng*. 2014;9(8):213–220.
119. Butkus S, Gaižauskas E, Paipulas D, Viburys Z, Kaškelye D, Barkauskas M, Alesenkov A, Sirutkaitis V. Rapid microfabrication of transparent materials using filamented femtosecond laser pulses. *Appl Phys Mater Sci Process*. 2014;114(1):81–90.
120. Butkus S, Paipulas D, Kaškelytė D, Gaižauskas E, Sirutkaitis V. Improvement of cut quality in rapid-cutting of glass method via femtosecond laser filamentation. *J Laser Micro Nanoeng*. 2015;10(1):59–63.
121. Ahmed F, Lee MS, Sekita H, Sumiyoshi T, Kamata M. Display glass cutting by femtosecond laser induced single shot periodic void array. *Appl Phys Mater Sci Process*. 2008;93(1):189–192.
122. Werr F, Eppelt U, Müllers L, De Ligny L. Ultra-short-pulse laser filaments for float glass cutting: Influence of laser parameters on micro cracks formation. *Front Phys*. 2022;10:862419.
123. Li J, Ertorer E, Herman PR. Ultrafast laser burst-train filamentation for non-contact scribing of optical glasses. *Opt Express*. 2019;27(18):25078.
124. Yan T, Ji L, Li L, Amina, Wang W, Lin Z, Qiang Y. Submicron fine cutting-surface of sapphire obtained by chemical corrosion assisted picosecond laser fulmination technology. *Chin J Lasers*. 2017;44(10):Article 1002002.
125. Butkus S, Paipulas D, Viburys Ž, Alesenkov A, Gaižauskas E, Kaškelyte D, Barkauskas M, Sirutkaitis V. Rapid microfabrication of transparent materials using a filamented beam of the IR femtosecond laser. *Proc SPIE*. 2014;8972:Article 897216.
126. Miyamoto I, Cvecek K, Schmidt M. Advances of laser welding technology of glass -science and technology. *J Laser Micro Nanoeng*. 2020;15(2):63–76.
127. Tamaki T, Watanabe W, Nishii J, Itoh K. Welding of transparent materials using femtosecond laser pulses. *Jpn J Appl Phys*. 2005;44(5L):Article L687.
128. Chen J, Carter RM, Thomson RR, Hand DP. Avoiding the requirement for pre-existing optical contact during picosecond laser glass-to-glass welding. *Opt Express*. 2015;23(14):18645.
129. Zhang J, Chen S, Lu H, Huang M, Li J, Guo L, Lue Q, Zhang Q. *The effect of gap on the quality of glass-to-glass welding using a picosecond laser*. 2020;134: Article 106248.
130. Ozeki Y, Inoue T, Tamaki T, Yamaguchi H, Onda S, Watanabe W, Sano T, Nishiuchi S, Hirose A, Itoh K. Direct welding between copper and glass substrates with femtosecond laser pulses. *Appl Phys Express*. 2008;1(8):Article 082601.
131. Zhang G, Stoian R, Zhao W, Cheng G. Femtosecond laser Bessel beam welding of transparent to non-transparent materials with large focal-position tolerant zone. *Opt Express*. 2018;26(2):917.
132. Chambonneau M, Li Q, Fedorov VY, Blothe M, Schaarschmidt K, Lorenz M, Tzortzakis S, Nolte S. Taming ultrafast laser filaments for optimized semiconductor–metal welding. *Laser Photonics Rev*. 2021;15(2): Article 2000433.